# Internal Rotation and Spin Conversion of $CH_3OH$ in Solid para-Hydrogen

Yuan-Pern Lee *et al.*

*Science* **311**, 365 (2006);
DOI: 10.1126/science.1121300

regation occurs during calcination to produce alloy nanoparticles having a Pd-rich shell surrounding a Au-rich core.

The catalytic data show that the introduction of Au to Pd improves selectivity, and we believe that the surface of the bimetallic nanoparticles will still contain some Au. Hence, we argue that the Au acts as an electronic promoter for Pd and that the active catalyst has a surface that is significantly enriched in Pd. Recent studies have started to provide insights into the nature of such effects. For example, Okazaki *et al*. (*27*) have shown, using a combination of experiment and theory, that the electronic structure of Au in $Au/TiO_2$ catalysts is dependent on the particle size, and Goodman and co-workers (*28*), using model studies, have shown that Au can isolate Pd sites within bimetallic systems.

**References and Notes**


1. R. A. Sheldon, J. K. Kochi, *Metal-Catalyzed Oxidations of Organic Compounds* (Academic Press, New York, 1981).
2. M. Beller, C. Bolm, *Transition Metals for Organic Synthesis* (Verlag GmbH & Co. KGaA, Weinheim, Germany, ed. 2, 2004).
3. G. ten Brink, I. W. C. E. Arends, R. A. Sheldon, *Science* **287**, 1636 (2000).
4. M. Vazylyev, D. Sloboda-Rozner, A. Haimov, G. Maayan, R. Neumann, *Top. Catal.* **34**, 93 (2005).
5. M. Pagliaro, S. Campestrini, R. Ciriminna, *Chem. Soc. Rev.* **34**, 837 (2005).
6. K. Mori, T. Hara, T. Mizugaki, K. Ebitani, K. Kaneda, *J. Am. Chem. Soc.* **26**, 10657 (2004).
7. I. E. Markó, P. R. Giles, M. Tsukazaki, S. M. Brown, C. J. Urch, *Science* **274**, 2044 (1996).
8. M. J. Schultz, R. S. Adler, W. Zierkiewicz, T. Privalov, M. S. Sigman, *J. Am. Chem. Soc.* **127**, 8499 (2005).
9. U. R. Pillai, E. Sahle-Demessie, *Appl. Catal. Gen.* **245**, 103 (2003).
10. M. Hudlicky, *Oxidations in Organic Chemistry* (American Chemical Society, Washington, DC, 1990).
11. W. P. Griffith, J. M. Joliffe, *Stud. Surf. Sci. Catal.* **66**, 395 (1991).
12. G. Cainelli, G. Cardillo, *Chromium Oxidants in Organic Chemistry* (Springer, Berlin, 1984).
13. D. G. Lee, U. A. Spitzer, *J. Org. Chem.* **35**, 3589 (1970).
14. F. M. Menger, C. Lee, *Tetrahedron Lett.* **22**, 1655 (1981).
15. R. Neumann, M. Levin-Elad, *Appl. Catal. A* **122**, 85 (1995).
16. L. Prati, M. Rossi, *J. Catal.* **176**, 552 (1998).
17. F. Porta, L. Prati, M. Rossi, G. Scari, *J. Catal.* **211**, 464 (2002).
18. S. Carretin, P. McMorn, P. Johnston, K. Griffin, G. J. Hutchings, *Chem. Commun.* **2002**, 696 (2002).
19. F. Porta, L. Prati, *J. Catal.* **224**, 397 (2004).
20. S. Biella, M. Rossi, *Chem. Commun.* **2003**, 378 (2003).
21. A. Abad, P. Conception, A. Corma, H. Garcia, *Angew. Chem.* **44**, 4066 (2005).
22. P. Landon, P. J. Collier, A. J. Papworth, C. J. Kiely, G. J. Hutchings, *Chem. Commun.* **2002**, 2058 (2002).
23. P. Landon *et al.*, *Phys. Chem. Chem. Phys.* **5**, 1917 (2003).
24. J. K. Edwards *et al.*, *J. Mater. Chem.* **15**, 4595 (2005).
25. J. K. Edwards *et al.*, *J. Catal.* **236**, 69 (2005).
26. To confirm that surface segregation of Pd was truly occurring in these nanoparticles, multivariate statistical analysis (MSA) was performed on the data set shown in Fig. 2B. MSA is a group of processing techniques that can be used to identify specific features within large data sets such as x-ray spectrum images and to reduce random noise components in the data sets in a statistical manner. MSA has recently been shown to be particularly useful for analysis of x-ray maps taken from nanoparticles (*29*). This statistical technique performs a data-smoothing calculation by portioning the XEDS data using a probability density function.
27. K. Okazaki, S. Ichikawa, Y. Maeda, M. Haruta, M. Kohyama, *Appl. Catal. A* **291**, 45 (2005).
28. M. Chen, D. Kumar, C.-W. Yi, D. W. Goodman, *Science* **310**, 291 (2005).
29. N. Bonnet, *J. Microsc.* **190**, 2 (1998).


30. Sponsored by the European Union AURICAT project (contract HPRN-CT-2002-00174) and the Engineering and Physical Sciences Research Council (EPSRC) as part of the ATHENA project co-sponsored by Johnson Matthey, as well as by an EPSRC-sponsored program on Speculative Green Chemistry, and we thank them for funding this research. We also thank the World Gold Council (through the GROW scheme) and Cardiff University (AA Reed studentship) for providing support for J.K.E. D.I.E. thanks the Crystal Faraday Partnership for funding. Finally, C.J.K., M.A.W., and A.A.H. gratefully acknowledge NSF funding through the Materials Research Science and Engineering Center (NSF grants DMR-0079996, DMR-0304738, and DMR-0320906).


**Supporting Online Material**

www.sciencemag.org/cgi/content/full/311/5759/362/DC1
Materials and Methods
Fig. S1

26 September 2005; accepted 7 December 2005
10.1126/science.1120560

# Internal Rotation and Spin Conversion of $CH_3OH$ in Solid para-Hydrogen

**Yuan-Pern Lee,[1,2]* Yu-Jong Wu,[3] R. M. Lees,[4] Li-Hong Xu,[4] Jon T. Hougen[5]**

**The quantum solid para-hydrogen ($p$-$H_2$) has recently proven useful in matrix isolation spectroscopy. Spectral lines of compounds embedded in this host are unusually narrow, and several species have been reported to rotate in $p$-$H_2$. We found that a $p$-$H_2$ matrix inhibits rotation of isolated methanol ($CH_3OH$) but still allows internal rotation about the C–O bond, with splittings of the *E*/*A* torsional doublet in internal rotation–coupled vibrational modes that are qualitatively consistent with those for $CH_3OH$ in the gaseous phase. This simplified high-resolution spectrum further revealed the slow conversion of nuclear spin symmetry from species *E* to species *A* in the host matrix, offering potential insight into nuclear spin conversion in astrophysical sources.**

In a quantum solid, the de Broglie wavelength of the species with small mass becomes a substantial fraction of its size at low temperature, resulting in delocalization of the nuclei. Because of the "softness" associated with the quantum solid properties of a $p$-$H_2$ matrix (*1*–*3*), guest molecules such as methane can rotate in solid $p$-$H_2$ more readily than in other matrices; the rotational parameters of species isolated in $p$-$H_2$ are typically ~90% of those for the gaseous phase, even less affected than the parameters of species in helium droplets (*4*, *5*). For larger species, molecular rotation is less likely to occur but internal rotation (torsion) of methyl groups could well persist.

The torsional motion itself is one representative of the class of large-amplitude molecular vibrational motions. In common with overall rotation, these vibrational motions involve displacements of atoms over distances comparable to chemical bond lengths, but in contrast to rotational motions, they are hindered by potential barriers reflective of some mixture of chemical bond properties and van der Waals repulsions.

Internal rotation typically couples with other vibrational modes to give a substantial variety of energy patterns. This coupling with torsional bath states is also believed to be the mechanism responsible for the large enhancement of intramolecular vibrational energy redistribution rates in methyl rotor–containing molecules. Spectral analysis of vibration-rotation bands involving internal rotation is often challenging, but the low-temperature solid $p$-$H_2$ environment ensures that nearly all absorption lines originate from the lowest levels. Moreover, fine structure is observable because the infrared (IR) absorption lines of guest molecules in the $p$-$H_2$ matrix can be extremely sharp, with full widths at half maximum (FWHM) less than 0.01 $cm^{-1}$ (*4*, *6*).

Here we apply the advantages of $p$-$H_2$ to vibrational spectroscopy of methanol. We have observed torsional tunneling splittings between the *A* and *E* symmetry species associated with internal rotation about the C–O bond, permitting a clear differentiation between the corresponding $I = 3/2$ and $I = ½$ nuclear spin modifications of the methyl hy-

[1]Department of Applied Chemistry and Institute of Molecular Science, National Chiao Tung University, 1001 Ta-Hsueh Road, Hsinchu 30010, Taiwan. [2]Institute of Atomic and Molecular Sciences, Academia Sinica, Taipei 10617, Taiwan. [3]Department of Chemistry, National Tsing Hua University, 101, Sec. 2, Kuang Fu Road, Hsinchu 30013, Taiwan. [4]Centre for Laser, Atomic and Molecular Sciences, Department of Physical Sciences, University of New Brunswick, 100 Tucker Park Road, Saint John, New Brunswick E2L 4L5, Canada. [5]Optical Technology Division, National Institute of Standards and Technology, Gaithersburg, MD 20899, USA.

*To whom correspondence should be addressed. E-mail: yplee@mail.nctu.edu.tw

drogens in $CH_3OH$. Monitoring the relative intensities in *A*/*E* transition pairs as a function of time thus permitted a determination of nuclear spin conversion rates in this molecule. Previously, the time dependence of structure associated with overall molecular rotation had been used to study spin conversion in water, methane, and ammonia in rare gas matrices (*7*–*9*). Spin conversion processes are of particular relevance in molecular astrophysics, wherein it remains unclear whether different symmetry species in astronomical sources should be viewed as independent molecular reservoirs with independent excitation temperatures, or instead should be treated as a whole and characterized by a common temperature. The question of how spin conversion is promoted by molecule-solid interactions on molecular ices also remains open.

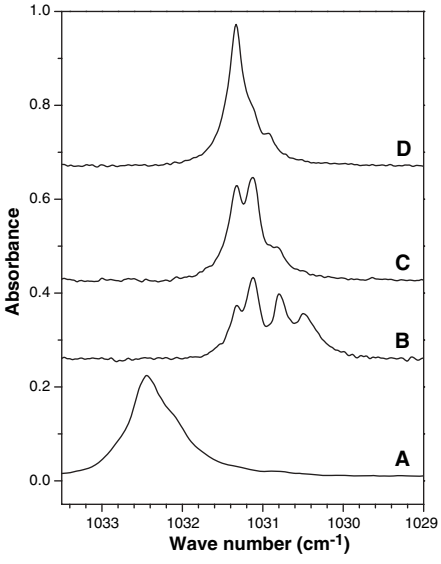


**Fig. 1.** Partial IR absorption spectra of the C–O stretching mode of matrix-isolated $CH_3OH$. (**A**) $CH_3OH$/Ne (1/5000). (**B**) $CH_3OH$/*p*-$H_2$ (1/5000) after deposition. (**C**) Annealing of $CH_3OH$/*p*-$H_2$ for 2 hours at 5 K. (**D**) Sample in (B) after 70 hours in darkness at 3.5 K. For each acquisition of spectral data, 200 scans corresponding to a resolution of 0.05 $cm^{-1}$ were accumulated. The acquisition process took ~1 hour, during which time the sample was held at 3.5 K.

In our experiments, a nickel-plated copper plate served both as a cold substrate for the matrix sample and as a mirror to reflect the incident IR beam to the detector. Typically, a gaseous mixture of $CH_3OH$/*p*-$H_2$ (1/5000 to 1/3000, 0.12 mol) was deposited over a period of 4 hours (*10*, *11*). IR absorption spectra were recorded with a Fourier-transform infrared (FTIR) spectrometer (Bomem, DA8) (*12*) equipped with a KBr beamsplitter and a Hg/Cd/Te detector (cooled to 77 K) to cover the spectral range 500 to 5000 $cm^{-1}$. Typically, 200 scans at a resolution of 0.05 $cm^{-1}$ were recorded at each stage of the experiment. The intense feature near 1030 $cm^{-1}$ associated with C–O stretching in the IR spectrum (*13*, *14*) was recorded with a $CH_3OH$/*p*-$H_2$ concentration of 1/5000; absorption lines attributed to other vibrational modes are much weaker and required higher concentration (~1/3000) to achieve a practical signal-to-noise ratio.

The IR spectrum of a sample of $CH_3OH$/Ne (1/5000) at 3.5 K exhibits a single broad line at 1032.45 $cm^{-1}$ with FWHM ~0.6 $cm^{-1}$ in the C–O stretching region (Fig. 1A). In contrast, the spectrum of $CH_3OH$/*p*-$H_2$ (1/5000) at 3.5 K exhibits multiple lines at ~1031 $cm^{-1}$ with FWHM ~0.15 $cm^{-1}$ (Fig. 1B). A *p*-$H_2$ matrix prepared with direct vapor deposition has a mixed crystal structure; annealing of the matrix near 5 K converts the matrix to a hexagonal close-packed structure (*4*). After sample annealing at 5 K for 2 hours, the original multiplet has evolved to a doublet at 1031.12 and 1031.31 $cm^{-1}$ (Fig. 1C). In separate experiments, we verified that this doublet can be obtained free from interference in the lower energy region only when the concentrations of $CH_3OH$ and *o*-$H_2$ impurity are low. The matrix also undergoes self-annealing at 3.5 K; nearby lines other than this doublet disappeared 40 hours after deposition even without annealing at a high temperature.

The observed doublet wavenumbers match closely with the known subband origins at 1033.707 and 1033.896 $cm^{-1}$ in gaseous $CH_3OH$ (Table 1) (*13*, *14*). Because of their relaxation behavior and wavenumber separation, these two transitions can be identified with transitions from the *E* and *A* components of the ground state ($\nu_i'' = 0$ for $i = 1$ to 12 and $K'' = 0$) to the *E* and *A* components of the upper state ($\nu_8' = 1$, $\nu_{12}' = 0$, and $K' = 0$) of the C–O stretching mode, where $\nu_8$ and $\nu_{12}$ are the C–O stretching and torsional quantum numbers, respectively. For simplicity, we denote observed transitions from the ground state by $n\nu_i$, where *n* is the vibrational quantum number of the upper state (omitted when $n = 1$) and $\nu_i$ is the vibrational mode. Although there is a matrix shift of –2.59 $cm^{-1}$, the *E*-*A* line separation of –0.19 $cm^{-1}$ observed for $\nu_8$ is identical to the value for gaseous $CH_3OH$. The spectrum of the matrix sample after 70 hours in the dark at 3.5 K (Fig. 1D) shows markedly increased intensity of the line at 1031.31 $cm^{-1}$ at the expense of line intensity at 1031.12 $cm^{-1}$. This variation of intensity shows that, in the *p*-$H_2$ matrix, the molecules of *E* symmetry slowly convert to the *A* species (with an energy decrease of ~9 $cm^{-1}$) (*14*), a process that can only occur via conversion of the $CH_3$ total nuclear spin from $I = ½$ to $I = 3/2$. Fitting of a single-exponential decay (or rise) of six data points between 40 and 70 hours for component *E* (or *A*) yields a rate coefficient for the spin conversion from *E* to *A* components at 3.5 K of ~0.018 ± 0.003 $hour^{-1}$.

Because there are no obvious lines remaining in the C–O stretching region to assign to

**Table 1.** Comparison of line positions between $CH_3OH$ isolated in solid *p*-$H_2$ and in the gaseous phase. Matrix shift is defined as $\Delta = \nu_{matrix} - \nu_{gas}$.

| Mode | Description | Symmetry | Gas phase | | This work§ | | Matrix shift |
|---|---|---|---|---|---|---|---|
| | | | $cm^{-1}$ | Δ(*E*-*A*) | $cm^{-1}$ | Δ(*E*-*A*) | |
| $\nu_2$ | C–H asymmetrical stretch | *E* | 2994.60* | –12.39 | 2995.61 | –7.62 | 1.01 |
| | | $A_1$ | 3006.99 | | 3003.23 | | –3.76 |
| $\nu_3$ | C–H symmetrical stretch | *E* | 2844.66* | –0.06 | 2840.66 | <0.1 | –4.00 |
| | | $A_1$ | 2844.72 | | 2840.66 | | –4.06 |
| $\nu_7$ | $CH_3$ rock | *E* | 1070.31† | –4.57 | 1073.69 | –1.33 | 3.38 |
| | | $A_1$ | 1074.884 | | 1075.02 | | 0.14 |
| $\nu_8$ | C–O stretch | *E* | 1033.707† | –0.189 | 1031.12 | –0.19 | –2.59 |
| | | $A_1$ | 1033.896 | | 1031.31 | | –2.59 |
| $\nu_9$ | C–H asymmetrical stretch | *E* | 2952.04* | –14.61 | 2951.72 | –14.14 | –0.32 |
| | | $A_2$ | 2966.65 | | 2965.86 | | –0.79 |
| $2\nu_4$ | Overtone | *E* | 2957.57‡ | –0.79 | 2956.50 | –0.54 | –1.07 |
| | | $A_1$ | 2958.36 | | 2957.04 | | –1.32 |

*$K = 0$ subband origins determined from the term values given in (*16*). †From (*13*, *14*). ‡From (*22*). §All measurements are estimated to have type B uncertainties ($k = 2$) (*23*) of ± 0.05 $cm^{-1}$ or better.

transitions arising from the $J = K = 1$ level of methanol (~5 $cm^{-1}$ above the $J = K = 0$ level), we conclude that methanol does not rotate about its principal $a$ axis in the $p$-$H_2$ matrix. This finding is in contrast to earlier observations of rotational structure for water, methane, and ammonia in rare-gas matrices (*7*–*9*) and seems somewhat surprising given that nearly free rotation in $p$-$H_2$ is exhibited by methane, which has a moment of inertia for rotation about its $C_3$ axis only slightly smaller than that of methanol about the C–O bond axis. Nonetheless, if we assume that methanol cannot carry out overall rotations but can carry out internal rotations, this raises the question of how the internal rotation splittings are affected by the $p$-$H_2$ matrix. Given that internal rotation splitting in the C–O stretching fundamental in $p$-$H_2$ is nearly identical to the gas-phase value (Table 1), it appears that the matrix alters neither the potential barrier $V_3$ nor the effective internal-rotation constant $F$ for this mode. If true, this might imply that studies of the simple rotation-free transitions in a $p$-$H_2$ matrix could greatly aid in sorting out the complex gas-phase spectra of methanol. Currently, there is a lack of experimental information about the important low-$J$ and low-$K$ assignments for many of the methanol vibrational fundamentals; hence, insights from the $p$-$H_2$ experiments would be extremely valuable.

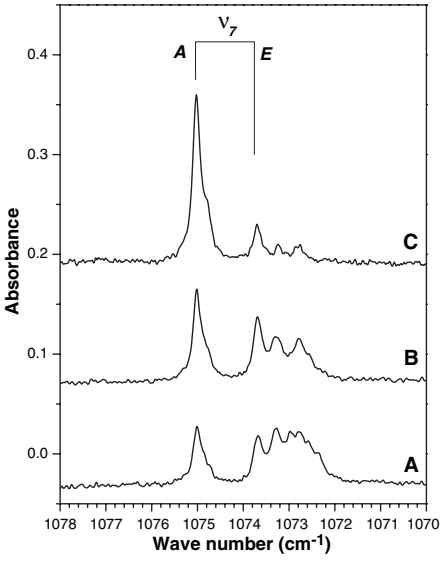


**Fig. 2.** Partial IR absorption spectra of in-plane $CH_3$-rocking mode of a $CH_3OH/p$-$H_2$ (1/3000) matrix sample, acquired (**A**) after deposition at 3.5 K, (**B**) after annealing the sample for 2 hours at 5 K, and (**C**) after 70 hours in darkness at 3.5 K. Conditions of data acquisition are the same as for Fig. 1.

Our spectra for the in-plane $CH_3$-rocking ($\nu_7$) mode of $CH_3OH$ in the region 1070 to 1078 $cm^{-1}$ are shown in Fig. 2; traces A to C correspond respectively to $CH_3OH/p$-$H_2$ after deposition, after annealing, and 70 hours after deposition. The growing line at 1075.02 $cm^{-1}$ is assigned in Table 1 as the $A$ component of the $\nu_7$ band, very close to the gas-phase value of 1074.884 $cm^{-1}$ (*13*). However, the best candidate for the $E$ component lies at 1073.69 $cm^{-1}$, distinctly higher than the reported gas-phase value of 1070.31 $cm^{-1}$ (*13*). Thus, our $E$-$A$ line separation of –1.33 $cm^{-1}$ in Table 1 is smaller than the value of –4.57 $cm^{-1}$ for the gas phase. The rate coefficient for conversion from our assigned $E$ component to the $A$ component at 3.5 K is ~0.019 ± 0.002 $hour^{-1}$, consistent with the rate derived from the $\nu_8$ mode.

The $\nu_2$, $\nu_9$, $2\nu_4$, and $\nu_3$ bands have been characterized in the C–H stretching region of the vibration-rotational spectrum of gaseous $CH_3OH$ (*15*, *16*). The $K = 0$, $A$ subband and $K = 0$, $E$ subband origins deduced from the upper-state term values are listed in Table 1. The $A/E$ splittings are less than 0.8 $cm^{-1}$ for $2\nu_4$ and $\nu_3$ but increase to 12.4 $cm^{-1}$ and 14.6 $cm^{-1}$ for $\nu_2$ and $\nu_9$, respectively. In the spectrum of $CH_3OH$/Ne in the region 2800 to 3030 $cm^{-1}$ (Fig. 3A), no splitting was observed. The spectrum of $CH_3OH/p$-$H_2$ 70 hours after deposition (Fig. 3C) exhibits a pattern similar to that for $CH_3OH$ in the gaseous phase: no splitting for the strong $\nu_3$ line at 2840.66 $cm^{-1}$ nor for the $2\nu_4$ feature at 2956.77 $cm^{-1}$, but large splittings for lines assigned to $\nu_2$ at 3003.23 $cm^{-1}$ (*A*) and 2995.61 $cm^{-1}$ (*E*) and to $\nu_9$ at 2965.86 $cm^{-1}$ (*A*) and 2951.72 $cm^{-1}$ (*E*).

A further sharp doublet can be seen at 2916.92 and 2914.97 $cm^{-1}$ (Fig. 3C). The temporal behavior of the relative intensities clearly indicates that the former is the $A$ component and the latter the $E$ component. A weaker line at 2933.02 $cm^{-1}$ can also be identified as a transition of $A$ symmetry. The corresponding bands for $CH_3OH$ in the gaseous phase have not been unambiguously identified, but from considerations of symmetry, wavenumber, and analogy with model predictions for the $\nu_4$ and $\nu_5$ $CH_3$-bending fundamentals, we can tentatively associate the lines at 2916.92 $cm^{-1}$ and 2933.02 $cm^{-1}$ in the $p$-$H_2$ matrix with the $2\nu_5$ overtone and the $\nu_4 + \nu_5$ combination band, respectively.

The remaining vibrational fundamentals are the $\nu_1$ OH-stretching mode around 3680 $cm^{-1}$ (*17*); the $\nu_4$, $\nu_5$, and $\nu_{10}$ $CH_3$-bending modes around 1470 $cm^{-1}$ (*18*); the $\nu_6$ OH-bending mode around 1340 $cm^{-1}$ (*19*); and the $\nu_{11}$ out-of-plane $CH_3$-rocking mode around 1280 $cm^{-1}$ (*20*). The experimental situation at $K = 0$ for the gas-phase spectra of several of these bands is still very uncertain. No low-$K$ subbands have been assigned for the three $CH_3$-bending fundamentals (*18*), nor for the $\nu_{11}$ rocking band (*20*). The OH-bending mode lies in a complex region of strong mixing with other torsional combination states, and the correct vibrational labeling of the rotationally assigned $K = 0$ subbands is not clear, leaving a number of $U$ subbands unidentified (*19*).

Our observed spectra for methanol in $p$-$H_2$ clearly show additional splitting structure in all of the above regions. Comparison with the experimental or predicted gas-phase subband origins indicates matrix shifts of less than 10 $cm^{-1}$ for all of the fundamentals (excluding the torsion) and internal rotation splittings in general qualitative agreement. In particular, a strong single peak at 1449.16 $cm^{-1}$ that grows with annealing is in good agreement with the predicted 1453.4/1453.1 $cm^{-1}$ for the $\nu_5$ $A/E$ doublet (*18*), and a strong peak clearly of $A$ symmetry at 1364.43 $cm^{-1}$ is consistent with the $U_0$ subband reported at 1369.69 $cm^{-1}$. This band, rather than the published 1320.63 $cm^{-1}$ assignment (*19*), could actually correspond to the $\nu_6$ OH-bending $K = 0$, $A$ subband. However, we consider

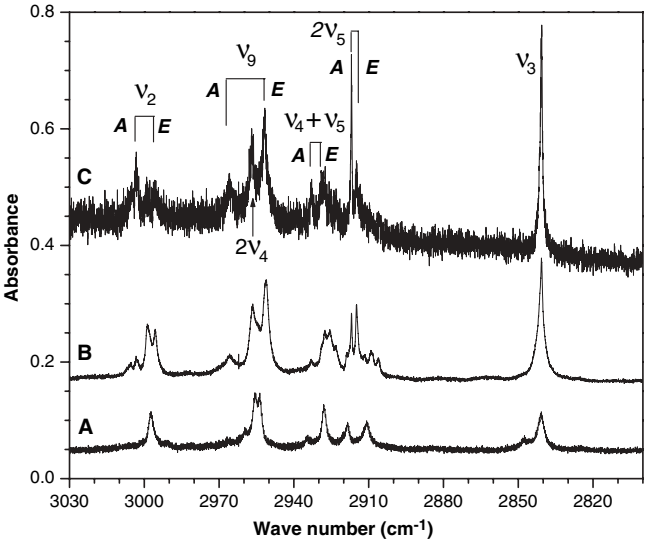


**Fig. 3.** Partial IR absorption spectra of the C–H stretching region of matrix-isolated $CH_3OH$. (**A**) $CH_3OH$/Ne (1/3000). (**B**) $CH_3OH/p$-$H_2$ (1/3000) after deposition at 3.5 K. (**C**) Sample in (B) after 70 hours in darkness at 3.5 K. For each data acquisition, 200 scans corresponding to a resolution of 0.05 $cm^{-1}$ were accumulated. The acquisition process took ~1 hour, during which time the sample was held at 3.5 K. The effective spectral resolution is 0.09 $cm^{-1}$ because of the size of the aperture used.

that firm conclusions about the effects of the $p$-$H_2$ matrix on the methanol torsion-vibration spectral structure would be premature at this stage without more definitive gas-phase data.

Taken together, these results suggest that the $p$-$H_2$ matrix will serve as an important medium for the study of large-amplitude vibrational motions and molecular spin conversion processes, providing valuable information to aid our understanding of complicated spectral patterns both in the gas phase and in molecular ices.

**References and Notes**


1. T. Oka, *Annu. Rev. Phys. Chem.* **44**, 299 (1993).
2. T. Momose, T. Shida, *Bull. Chem. Soc. Jpn.* **71**, 1 (1998).
3. K. Yoshioka, D. T. Anderson, *J. Chem. Phys.* **119**, 4731 (2003).
4. S. Tam *et al.*, *J. Chem. Phys.* **111**, 4191 (1999).
5. T. Momose *et al.*, *J. Chem. Phys.* **103**, 1400 (1995).
6. T. Momose *et al.*, *J. Chem. Phys.* **107**, 7707 (1997).
7. R. L. Redington, D. E. Milligan, *J. Chem. Phys.* **39**, 1276 (1963).
8. F. H. Frayer, G. E. Ewing, *J. Chem. Phys.* **48**, 781 (1968).
9. H. P. Hopkins, R. F. Curl, K. S. Pitzer, *J. Chem. Phys.* **48**, 2959 (1968).
10. We have developed a pulsed-deposition technique that can operate at a deposition temperature up to 5.5 K (*21*). Thus, it is suitable for use with our previous cryogenic refrigerator that cools to only ~5 K. As well, with a new closed-cycle refrigerator system (Janis RDK-415) capable of cooling the sample target to 3.5 K, we could use conventional continuous deposition with a flow rate of ~0.03 mol hour$^{-1}$.
11. $CH_3OH$ (99.9%, Mallinckrodt, analytical reagent grade) was purified by passing the vapor though $P_2O_5$ to remove trace water impurity. $H_2$ (99.9999%, Scott Specialty Gases) was used after passage through a trap at 77 K before conversion to $p$-$H_2$. The $p$-$H_2$ converter comprised a copper cell filled with $Fe(OH)_3$ catalyst and cooled with a closed-cycle refrigerator. The efficiency of conversion is controlled by the temperature of the catalyst; at 15 K, the concentration of $o$-$H_2$ is ~100 ppm.
12. Any mention of commercial products in this paper is for information only; it does not imply recommendation or endorsement by NIST.
13. L.-H. Xu *et al.*, *J. Mol. Spectrosc.* **228**, 453 (2004).
14. G. Moruzzi, B. P. Winnewisser, M. Winnewisser, I. Mukhopadhyay, F. Strumia, *Microwave, Infrared and Laser Transitions of Methanol: Atlas of Assigned Lines from 0 to 1258 cm$^{-1}$* (CRC Press, Boca Raton, FL, 1995).
15. L.-H. Xu *et al.*, *J. Mol. Spectrosc.* **185**, 158 (1997).
16. X. Wang, D. S. Perry, *J. Chem. Phys.* **109**, 10795 (1998).
17. I. Kleiner, G. T. Fraser, J. T. Hougen, A. S. Pine, *J. Mol. Spectrosc.* **147**, 155 (1991).
18. M. A. Temsamani, L.-H. Xu, R. M. Lees, *J. Mol. Spectrosc.* **218**, 220 (2003).
19. R. M. Lees *et al.*, *J. Mol. Spectrosc.* **228**, 528 (2004).
20. R. M. Lees, L.-H. Xu, *Phys. Rev. Lett.* **84**, 3815 (2000).
21. Y.-J. Wu, X. Yang, Y.-P. Lee, *J. Chem. Phys.* **120**, 1168 (2004).
22. X. Wang, D. S. Perry, L.-H. Xu, unpublished data.
23. B. N. Taylor, C. E. Kugatt, *NIST Tech. Note 1297* (1994).


24. Supported by the Natural Sciences and Engineering Research Council of Canada (R.M.L. and L.H.X.) and by National Science Council of Taiwan grant NSC94-2113-M-009-017.

12 October 2005; accepted 12 December 2005
10.1126/science.1121300


# Formation of Glaciers on Mars by Atmospheric Precipitation at High Obliquity


**F. Forget,[1]* R. M. Haberle,[2] F. Montmessin,[3] B. Levrard,[4] J. W. Head[5]**



**Surface conditions on Mars are currently cold and dry, with water ice unstable on the surface except near the poles. However, geologically recent glacierlike landforms have been identified in the tropics and the midlatitudes of Mars. The ice has been proposed to originate from either a subsurface reservoir or the atmosphere. We present high-resolution climate simulations performed with a model designed to simulate the present-day Mars water cycle but assuming a 45° obliquity as experienced by Mars a few million years ago. The model predicts ice accumulation in regions where glacier landforms are observed, on the western flanks of the great volcanoes and in the eastern Hellas region. This agreement points to an atmospheric origin for the ice and reveals how precipitation could have formed glaciers on Mars.**


Among the most striking recent observations by the cameras aboard the Mars Express, Mars Global Surveyor (MGS), and Mars Odyssey orbiters are low-latitude, geologically recent, morphological features that clearly formed by the action of a water ice glacier (*1*–*8*). The most characteristic landforms appear to be clustered in several specific regions that had already been identified in Viking images (*9*, *10*). First, each of the Tharsis Montes volcanoes has a fan-shaped deposit near its northwestern flank (Fig. 1A), interpreted to be the remains of geologically recent glaciers (*3*, *4*). In the same region, debris-covered piedmont glaciers along the northwest edge of the Olympus Mons scarp (Fig. 1A) were seen in Viking and Mars Odyssey Thermal Emission Imaging System (THEMIS) data (*8*, *10*). Recent images of these glacier remnants obtained by the Mars Express High Resolution Stereo Camera (HRSC) show that they are covered by very recent rock glaciers (*1*, *2*). A second notable region is a relatively small area (1000 km across) on the eastern side of the Hellas Basin (90° to 120°E and 32° to 50°S), where some of the most spectacular examples of ice-related landforms are seen. More than 90 large lobate debris aprons up to 50 km across have been identified there (*5*, *9*). Some of these debris aprons are interpreted to represent very ice-rich debris-covered glaciers (*1*). Eastern Hellas also contains a variety of smaller ice-rich flow features, including tongue-shaped lobes observed at 247°W 38.6°S (*6*), hourglass-shaped craters apparently filled by a flowing debris-covered glacier (*1*), and many of the ice-cemented mantling deposits associated with gullies (*11*). A third major area of icy Mars is the Deuteronilus–Protonilus Mensae region (0° to 80°E and 30° to 50°N) (*9*), where large concentrations of lobate debris aprons and lineated valley fills (that resemble flow lines in glacial ice on Earth) are found. Outside these three regions, glacier-like features have been observed at mid-latitudes (*7*, *9*) but in more localized or limited forms.

Where did the ice come from? It has been suggested that the features could have been emplaced by creep or a landslide of material rich in ground ice (*12*, *13*) or released from a subsurface ground ice or groundwater reservoir (*2*). A recent analysis of the HRSC images of the western edge of Olympus Mons (*2*) concluded that the observations yielded evidence for hydrothermal mobilization of water with subsequent development of glaciers. However, the geomorphologic characteristic of most glacier features is also consistent with an atmospheric precipitation origin (*1*, *3*, *4*, *7*, *8*). This hypothesis has been supported by climate model simulations that suggested that, during a period of obliquity greater than about 35° to 45° (obliquity is the tilt of the planet's spin axis), the north polar water ice may be mobilized southward and deposited at lower latitudes (*14*–*16*). However, the simple cloud ice microphysics and the coarse spatial resolutions used by these previous models did not allow a true comparison between the modeled ice accumulations and the available geological observations.


[1]Laboratoire de Météorologie Dynamique, Institut Pierre Simon Laplace, Université Paris 6 Boite Postale 99, 75252 Paris cedex 05, France. [2]Space Science Division, Mail Stop 245-3, NASA Ames Research Center, Moffett Field, CA 94035, USA. [3]Service D'Aéronomie, Institut Pierre Simon Laplace, Université Paris 6 Box Postale 102, 75252 Paris cedex 05, France. [4]Astronomie et Systèmes Dynamiques, Institut de Mécanique Céleste, 77 Avenue Denfert Rochereau, 75014 Paris, France. [5]Department of Geological Sciences, Brown University, Providence, RI 02912, USA.

*To whom correspondence should be addressed. E-mail: forget@lmd.jussieu.fr